materials

MDPI

Communication

Facile Solvothermal Synthesis of $CuCo_2S_4$ Yolk-Shells and Their Visible-Light-Driven Photocatalytic Properties

Yinxia Chen [1], Xianbing Ji [1,*], Vadivel Sethumathavan [2,*] and Bappi Paul [3]

1 Hebei University of Environmental Engineering, Qinhuangdao 066102, China; chyxsd@163.com
2 Department of Chemistry, PSG College of Technology, Coimbatore 641004, India
3 Department of Chemistry, National Institute of Technology, Silchar, Assam 788010, India; bappipaulnits@gmail.com
* Correspondence: jixianbing1981@sina.com (X.J.); vlvelu7@gmail.com (V.S.)

Received: 11 October 2018; Accepted: 10 November 2018; Published: 16 November 2018

Abstract: In this present work, we synthesized a yolk-shell shaped $CuCo_2S_4$ by a simple anion exchange method. The morphological and structural properties of the as-synthesized sample were characterized using X-ray diffraction (XRD), UV-vis diffuse reflectance spectra (UV-vis DRS), scanning electron microscopy (SEM), and transmission electron microscopy (TEM). The SEM and TEM results confirmed that the uniform yolk-shell structure was formed during the solvothermal process. The band gap was about 1.41 eV, which have been confirmed by UV–vis DRS analysis. The photocatalytic property was evaluated by the photocatalytic degradation of methylene blue (MB) dye as a target pollutant under the visible-light irradiation. The experimental results confirmed the potential application of yolk-shell shape $CuCo_2S_4$ in visible-light photocatalytic applications.

Keywords: yolk-shell; structural; electron microscopy; semiconductors; photocatalyst

1. Introduction

Owing to their unique structural properties, as well as outstanding electrical properties, hollow nanostructures with tunable shape and size have gained huge research interest in the field of supercapacitors, catalysis, and biosensors [1]. The hollow architectures have relatively less density, high porosity, fast electron transfer, and higher surface area than the bulk materials. Up to date, various hollow structured metal oxides and sulfides have been successfully synthesized using soft and hard-template techniques [2]. For example, Y. Chen et al. fabricated Co_3O_4 hollow microspheres using Polyvinylpyrrolidone (PVP) as a template [3]. This synthesized hollow Co_3O_4 exhibits superior lithium storage capacity than the bulk Co_3O_4. S.E. Moosavifard et al. synthesized $CuCo_2O_4$ hollow spheres using a simple soft template route, which exhibits superior electrochemical than the bulk $CuCo_2O_4$ [4]. However, little attention has been paid by the research community to investigate the structural property of hollow metal sulfides [5]. In the past few decades, ternary metal sulfides have attracted great attention in the field of energy storage devices and photocatalysts due to their outstanding electrical properties. Among them, copper-cobalt sulfides ($CuCo_2S_4$) have been recognized as a promising material for pollutants degradation and water splitting, since they offer superior stability than other metal sulfides. $CuCo_2S_4$ is considered to be an environmentally benign material compared to CdS and In_2S_3 due to its low cost, less toxicity, and availability in nature [6]. In the past few decades, various morphologies of $CuCo_2S_4$, such as flowers, particles, and clusters have been successfully prepared using various approaches. In this work, we report a solvothermal route to synthesize a novel yolk-shell shaped $CuCo_2S_4$ using the sulfidation of Cu-Co glycerate precursor with thiourea. The prepared

$CuCo_2S_4$ yolk-shell exhibited superior photocatalytic activity towards the degradation of MB dye under the visible light without the aid of co-catalysts. To the best of our knowledge, this is the first report on the synthesis of $CuCo_2S_4$ yolk-shells and applications in visible-light-driven photocatalysts.

2. Experimental Section

In a typical synthesis, 35 mg of Cu $(NO_3)_2 \cdot 3H_2O$, 72 mg of Co $(NO_3)_2 \cdot 6H_2O$ was dissolved in a mixture of 7 mL of glycerol and 40 mL of isopropanol to form a clear solution. Then the solution was stirred for 1 h at room temperature and transferred into a Teflon-lined autoclave vessel and kept at 180 °C for 6 h in a muffle furnace. After cooling, the brown precipitate was washed thrice with ethanol and dried in a vacuum oven at 70 °C for 2 h and named as copper-cobalt glycerate precursor (Cu-Co glycerate). For the preparation of $CuCo_2S_4$ yolk-shell architectures, 30 mg of the Cu-Co-glycerate precursor was re-dispersed in 20 mL of ethanol solution, followed by the addition of 60 mg of thiourea. Then the mixture was transferred into a Teflon-lined autoclave and heated to 200 °C for 2 h. Finally, the black color product was washed with acetone several times, to obtain the $CuCo_2S_4$ (named as amorphous $CuCo_2S_4$). To improve the crystallinity, the final product was calcined at 300 °C for 30 min under air atmosphere (named as crystalline $CuCo_2S_4$).

Materials Characterization

Crystallinity and phase purity were examined by X-ray powder diffraction (X'pert-PRO-PANalytical X-ray diffractometer operated at 40 Kv). The microstructures and morphologies of the $CuCo_2S_4$ were characterized using a scanning electron microscope (SEM: Zeiss EVO 18 electron microscope, Germany) and transmission electron microscopy (TEM: JEOL-JEM 2100, USA). Elemental mapping of the yolk-shell architectures was analyzed using the EDX attached to the TEM instrument. The UV-vis diffuse reflectance spectra (DRS) were analyzed using a JASCO spectrophotometer (V-750, Japan), using $BaSO_4$ as a reference. The photocurrent measurements were recorded using a CHI660B workstation with a three-electrode configuration system. Then, 0.25 M Na_2SO_4 electrolytewas used for photocurrent measurements. The photocatalytic degradation of MB aqueous dye was carried out at room temperature under the visible-light irradiation of a 300 W tungsten halogen lamp. Then, 50 mg of catalyst and 50 mL of MB solution (10 ppm) was used for the photocatalytic degradation. At given intervals of illumination, the samples of the reaction solution were taken out, centrifuged, and analyzed using the JASCO UV-vis spectrophotometer.

3. Results and Discussion

The XRD pattern (Figure 1a) shows that all the diffraction peaks can be matched to the cubic phase of $CuCo_2S_4$ (crystalline) with JCPDS card No. 42-1450 [7]. Any other impurity peaks and secondary phases were observed, indicating that the Cu-Co-glycerate precursor was completely transferred to the $CuCo_2S_4$ phase after the sulfidation process with thiourea. According to the Scherrer calculation, the average crystalline size of $CuCo_2S_4$ was calculated to be 12 nm. The XRD pattern of amorphous $CuCo_2S_4$ (without calcination) did not show any prominent peaks indicating the poor crystalline nature of the material. Figure 1b shows the UV-vis DRS patterns of as-prepared $CuCo_2S_4$, which provides imperative evidence of their visible light photocatalytic performance. Apparently, the $CuCo_2S_4$ sample exhibited strong photo absorption in the entire visible light region. Using the Tauc plot of $(\alpha h\nu)^{1/2}$ vs. photon energy ($h\nu$), the band gap value for the $CuCo_2S_4$ yolk-shell was calculated to be 1.41 eV, respectively. SEM analysis was employed to investigate the morphology and the detailed structural property of the $CuCo_2S_4$ yolk-shells. SEM images from Figure 2a indicating a well-preserved spherical morphology with average diameters of about 1μm were observed. The interior structure of the yolk-shell structure was further investigated by TEM analysis. As shown in Figure 2d,e, the TEM images revealed that the $CuCo_2S_4$ composed of many hollow spherical shells with a relatively darker core could be observed in each of the spheres (Figure 2c). Moreover, the amorphous $CuCo_2S_4$ did not show any uniform yolk-shell formation. Furthermore,

the selected area electron diffraction (SAED) pattern (the inset of Figure 2e) determined that the yolk-shell $CuCo_2S_4$ was existing in polycrystalline nature. The TEM observation clearly confirmed that the as-prepared $CuCo_2S_4$ yolk-shells consisted of a highly porous nature which may be beneficial for superior photocatalytic degradation. Furthermore, the EDS (Figure 3a–e) images clearly indicate that the Cu, Co, and S elements are uniformly distributed in the $CuCo_2S_4$ yolk-shells, as in Reference [8]. These unique yolk-shell structures possessed a porous structure with a large specific surface area, guaranteeing a large contact area between the dye and the photocatalyst. Moreover, the electron separation and transporting behavior of the excited electron-hole pairs in $CuCo_2S_4$ could be validated by photocurrent studies. An appreciable photocurrent value can generally originate from the enhanced charge transportation and separation efficiency of photo-generated carriers [9]. As outlined in Figure 3f, the $CuCo_2S_4$ yolk-shells show an obvious photocurrent value, which implies that the effective charge separation in the $CuCo_2S_4$ system may beneficial for superior photocatalytic activity.

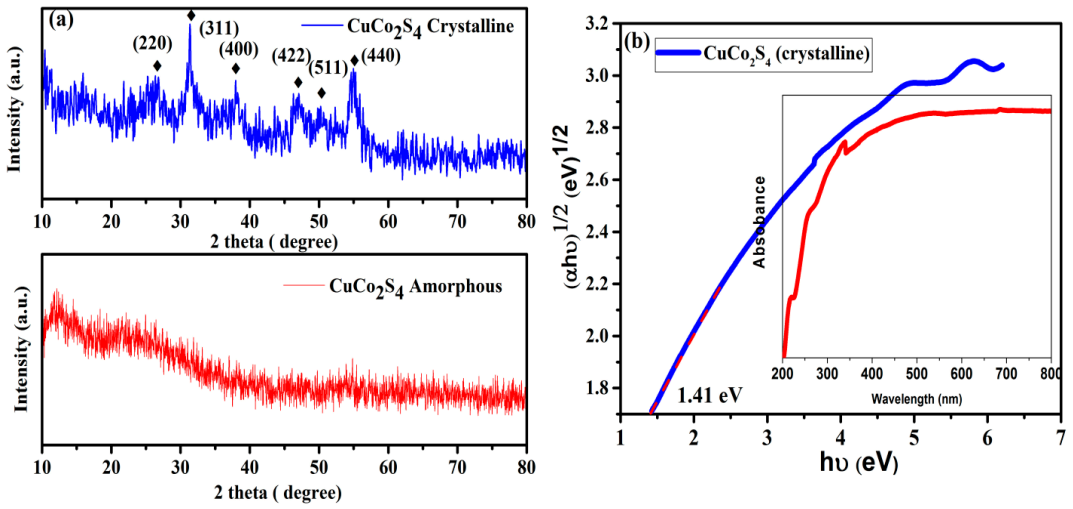

Figure 1. X-ray diffraction (XRD) patterns of (**a**) crystalline and amorphous $CuCo_2S_4$ (**b**) UV–vis diffuse reflectance spectra and $(\alpha h\nu)^2$ versus $h\nu$ plots of crystalline $CuCo_2S_4$.

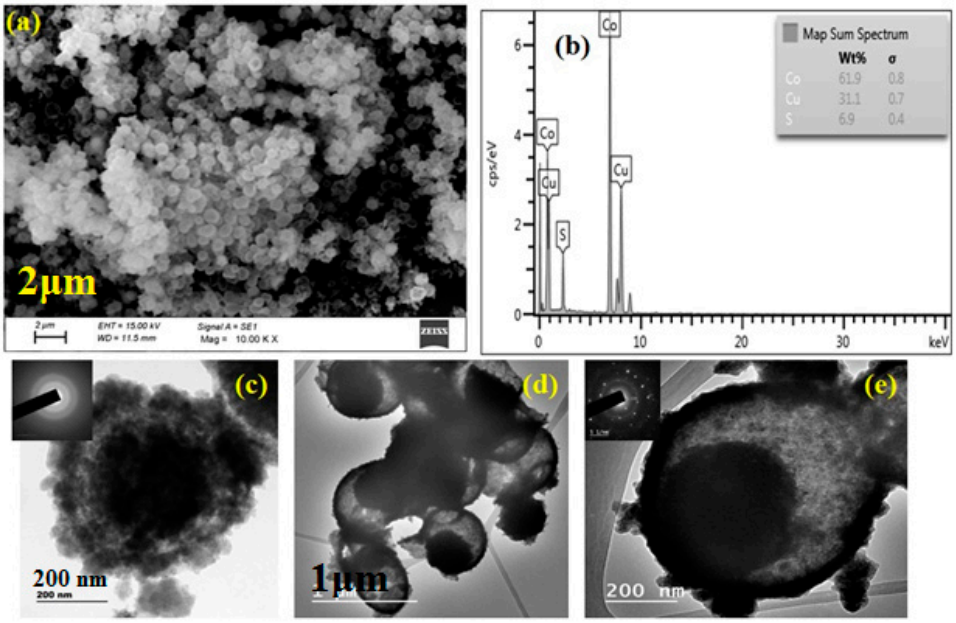

Figure 2. (**a**) Scanning electron microscopy (SEM) images (**b**) EDS spectra of $CuCo_2S_4$ yolk-shell structure (**c**) Transmission electron microscopy (TEM) images of amorphous $CuCo_2S_4$ (**d**,**e**) crystalline $CuCo_2S_4$ yolk-shell.

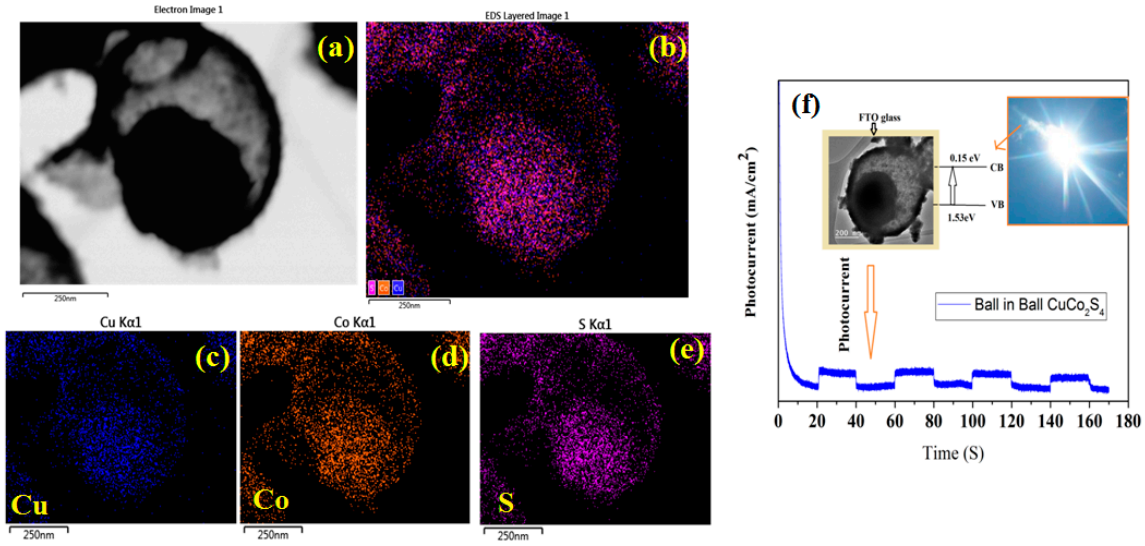

Figure 3. (**a**–**e**) EDS mapping (**f**) Photocurrent studies of $CuCo_2S_4$ yolk-shell structure.

Photocatalytic properties of the $CuCo_2S_4$ sample were investigated using the degradation of methylene blue (MB) dye as a target pollutant, Figure 4 shows the photocatalytic degradation curves (C_t/C_0) in % of MB aqueous dye solution with crystalline and amorphous $CuCo_2S_4$ as visible-light photocatalyst. For the blank test without the aid of any photocatalysts, the concentration of MB dye was not changed during the entire period of visible-light irradiation. After adsorption-desorption attainment in the dark, the change in the concentration of MB dye was only about 16% for crystalline $CuCo_2S_4$ material which was higher than that of amorphous $CuCo_2S_4$ powder (about 8%). However, the visible-light degradation of the crystalline $CuCo_2S_4$ was 95% after the 45 min visible-light irradiation, whilst that for the amorphous $CuCo_2S_4$ photocatalyst degraded only 38% after 45 min light irradiation [10–12]. Hence, crystalline $CuCo_2S_4$ had a higher photocatalytic activity than amorphous $CuCo_2S_4$ towards the MB degradation due to its pronounced oxygen vacancy and higher surface area (Figures S1 and S2).

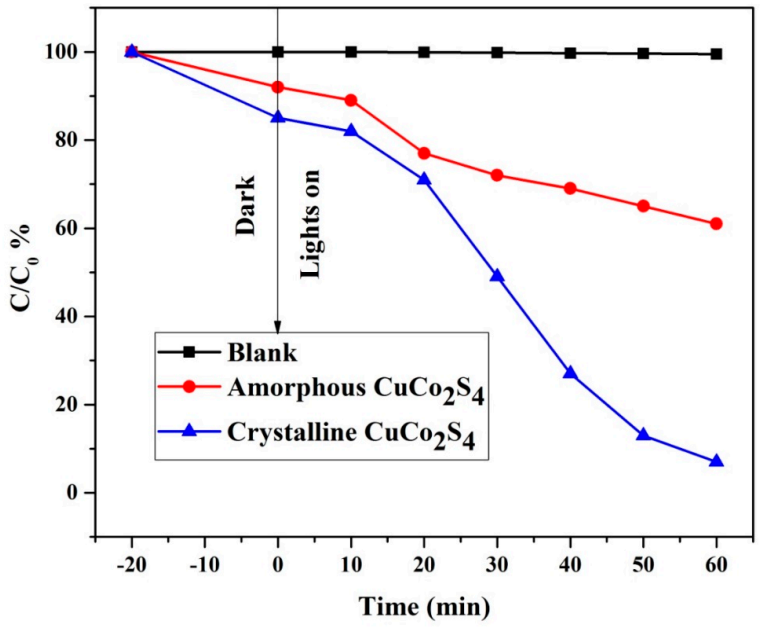

Figure 4. Photodegradation of MB with amorphous and crystalline $CuCo_2S_4$ under visible-light irradiation.

As shown in Figure 5a, $CuCo_2S_4$ was evaluated by varying the photocatalyst loadings from 25 to 75 mg at 10 mg L^{-1} of MB concentration. Initially, the degradation efficiency was increased with an increased number of catalytic loadings, which may be due to the availability of active sites for electron-hole pair generation. Beyond the 50 mg of photocatalyst loadings, the degradation efficiency was comparatively lower than the 50 mg loadings, which may be due to reduced light penetration in the photocatalyst system. The effect of dye concentration on the photocatalytic properties of $CuCo_2S_4$ was studied by varying the concentrations from 5 mg L^{-1} to 20 mg L^{-1}, as shown in Figure 5b. It was observed that 5 mg L^{-1} of MB dye was completely degraded within 60 min. Beyond 10 mg L^{-1}, the degradation efficiency of $CuCo_2S_4$ was much lower, which may be due to higher concentration of dye molecules blocking light penetration in the photocatalytic system. Figure 5c shows that the degradation rate constant of MB over the mg loading of $CuCo_2S_4$ (25), $CuCo_2S_4$ (50), and $CuCo_2S_4$ (75), was 12, 15, and 25 $min^{-1} \times 10^{-4}$, respectively. Hence, the proper loading amount of $CuCo_2S_4$ (50%) photocatalytic showed higher photocatalytic activity than other loadings. In addition, as shown in Figure 6, the cycle test results illustrate that the crystalline $CuCo_2S_4$ had a lower loss in its activity after three cycles [13–20]. Therefore, crystalline $CuCo_2S_4$ yolk-shells powder would be an ideal candidate for visible-light photocatalytic applications. Some few examples of copper based photocatalyst materials and its comparison with the $CuCo_2S_4$ yolk-shells are shown in Table 1.

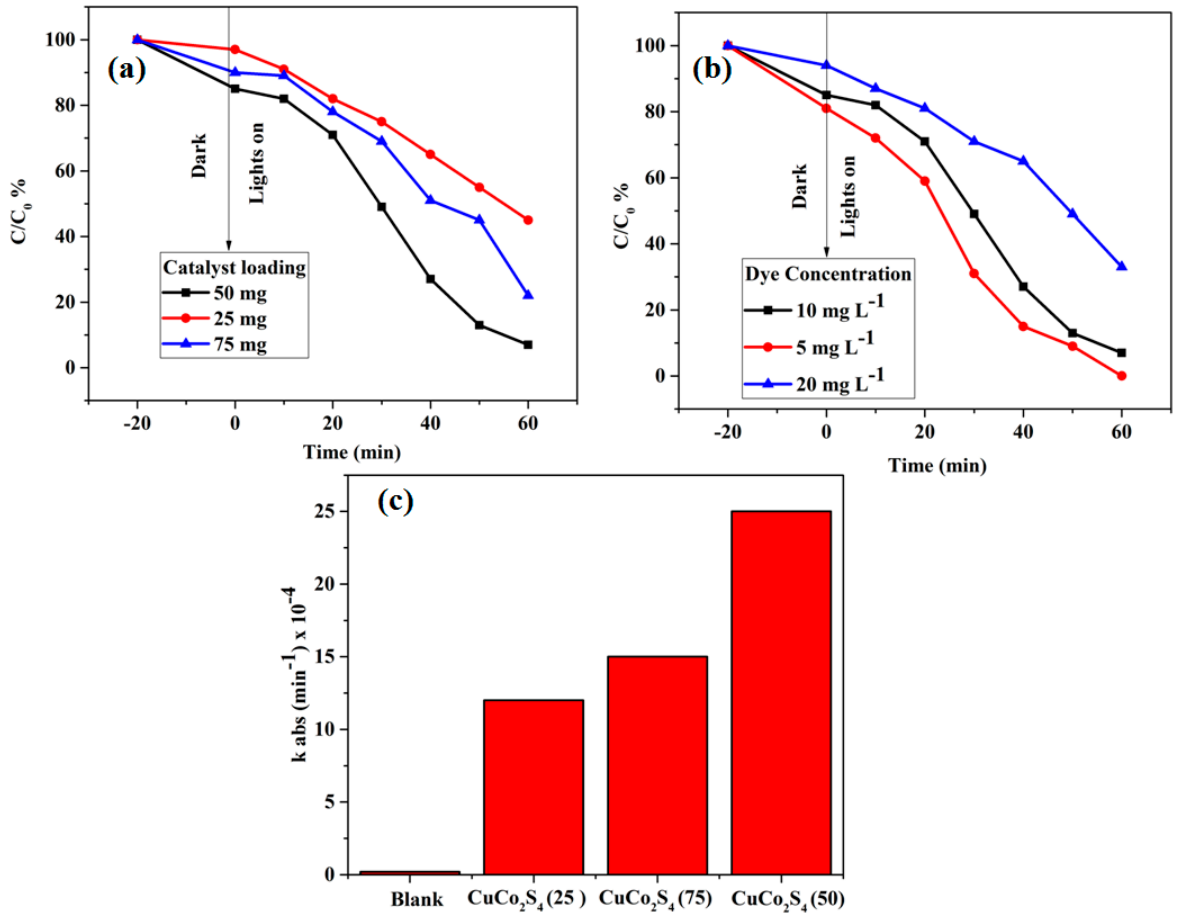

Figure 5. (**a**) Photodegradation of MB dye under different amounts of crystalline $CuCo_2S_4$ (**b**) different concentration of MB dye on $CuCo_2S_4$ (50 mg). (**c**) Degradation rate constant of MB over the $CuCo_2S_4$ yolk-shells loading.

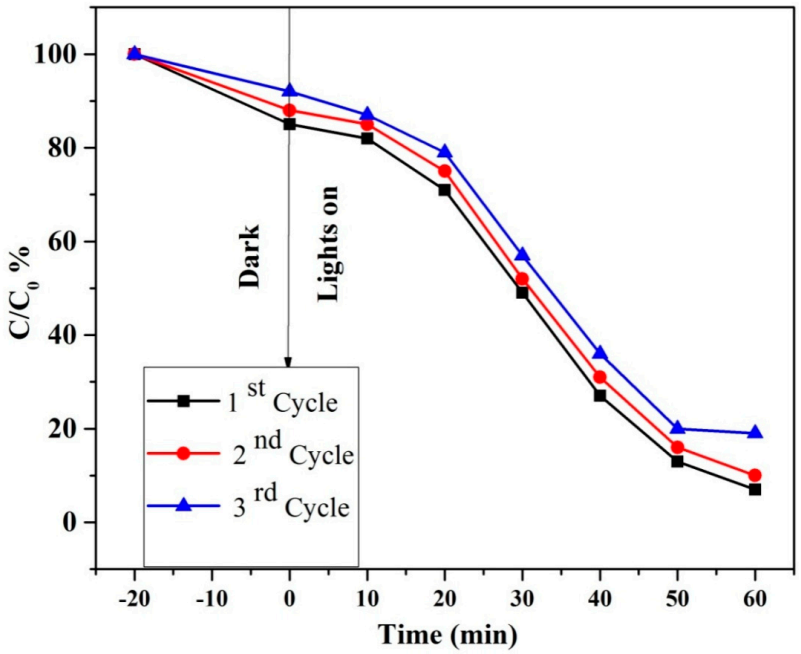

Figure 6. Cycle runs of MB photocatalytic degradation in the presence of crystalline $CuCo_2S_4$.

Table 1. Summary of photocatalytic performance of copper based photocatalyst materials.

S.No	Compound	Synthesis Method	Light Source	Dye	Conc mg L^{-1}	Catalyst Dosage	Irradiation Time	Efficiency	Ref.
1	Cu_2SnS_3	Solvothermal	100 W Xe Lamp	Methylene Blue	5	20 mg	240 min	N/A	[21]
2	Cu_2SnS_3	Solvothermal	150 W Tungsten–Halogen Lamp	Eosin	7.5	100 mg	140 min	N/A	[22]
3	Cu_2SnS_3	Hydrothermal	500 W Xe Lamp	Rhodamine B	10	100 mg	210 min	50%	[23]
4	$CuCo_2S_4$	Hydrothermal	500 W Tungsten–Halogen Lamp	Malachite Green	10	50 mg	360 min	40%	[24]
5	CoS_2	Hydrothermal	8 W Halogen Lamp	Methylene Blue	5	50 mg	120 min	N/A	[25]
6	Hexagonal Cu_2S copper sheets	N/A	300 W Xe Lamp	Rhodamine B	10	N/A	60 min	96%	[26]
7	Yolk-shell $CuCo_2S_4$	Ion exchange route	300 W Tungsten Halogen Lamp	Methylene Blue	10	50 mg	60 min	95%	This work

4. Conclusions

In summary, a simple solvothermal route was implemented for the preparation of $CuCo_2S_4$ yolk-shell structures. The UV-DRS spectra showed that the $CuCo_2S_4$ architectures had a broad visible-light absorption spectrum. The prepared $CuCo_2S_4$ yolk-shell structure exhibited good visible-light response and excellent photocatalytic activity towards the degradation of MB dye. The photocatalytic performances of the $CuCo_2S_4$ architectures were better than the previously reported degradation rate, which infers the potential applications of $CuCo_2S_4$. These results provided new insights that might lead to the development of $CuCo_2S_4$ yolk-shells for further application in the field of environmental remediation and energy storage devices, to utilize solar energy effectively.

Supplementary Materials: The following are available online at http://www.mdpi.com/1996-1944/11/11/2303/s1, Figure S1: BET spectrum of $CuCo_2S_4$ yolk-shells; Figure S2: XPS spectrum of $CuCo_2S_4$ yolk-shells; Figure S3: FT-IR spectrum of $CuCo_2S_4$ yolk-shells; Figure S4: SEM, TEM and EDX of amorphous $CuCo_2S_4$.

Author Contributions: Y.C., X.J. conceived, designed the experiments and wrote the paper, V.S. and B.P. analyzed the data and analysis tools.

Funding: This research received no external funding.

Acknowledgments: This work was funded by the Prominent Talent Project, Hebei University of Environmental Engineering (BJRC201701), the Project of Natural Science Foundation of Hebei Province (E2016415004, E2016415002), the Project of Science and Technology, Department of Hebei Province (15213629, 15213620), and the scientific research Project item of Hebei province education office (QN2016032).

Conflicts of Interest: The authors declare no conflict of interest.

References

1. Zhang, Y.; Zeng, W.; Ye, H.; Li, Y. Enhanced carbon monoxide sensing properties of TiO_2 with exposed (0 0 1) facet: A combined first-principle and experimental study. *Appl. Surf. Sci.* **2018**, *442*, 507–516. [CrossRef]
2. Li, Y.; Liu, T.; Li, T.; Peng, X. Hydrothermal fabrication of controlled morphologies of MoO_3 with CTAB: Structure and growth. *Mater. Lett.* **2015**, *140*, 48–50. [CrossRef]
3. Chen, Y.; Zhang, Y.; Fu, S. Synthesis and characterization of Co_3O_4 hollow spheres. *Mater. Lett.* **2007**, *61*, 701–705. [CrossRef]
4. Kaverlavani, S.K.; Moosavifard, S.E.; Bakouei, A. Self-templated synthesis of uniform nanoporous $CuCo_2O_4$ double-shelled hollow microspheres for high-performance asymmetric supercapacitors. *Chem. Commun.* **2017**, *53*, 1052–1055. [CrossRef] [PubMed]
5. Yu, L.; Wu, H.B.; Lou, X.W. Self-Templated Formation of Hollow Structures for Electrochemical Energy Applications. *Acc. Chem. Res.* **2017**, *50*, 293–301. [CrossRef] [PubMed]
6. Yan, Z.; Wu, H.; Han, A.; Yu, X.; Du, P. Noble metal-free cobalt oxide (CoO_x) nanoparticles loaded on titanium dioxide/cadmium sulfide composite for enhanced photocatalytic hydrogen production from water. *Int. J. Hydrogen Energy* **2014**, *39*, 13353–13360. [CrossRef]
7. Yinxia, C.; Xianbing, J.; Vadivel, S.; Paul, B. Anchoring carbon spheres on BiOBr/g-C_3N_4 matrix for high-performance visible light photocatalysis. *Ceram. Int.* **2018**, *44*, 23320–23323.
8. Kaur, A.; Umar, A.; Anderson, W.A.; Kansal, S.K. Facile synthesis of CdS/TiO_2 nanocomposite and their catalytic activity for ofloxacin degradation under visible illumination. *J. Photochem. Photobiol. A Chem.* **2018**, *360*, 34–43. [CrossRef]
9. Shen, L.; Yu, L.; Wu, H.B.; Yu, X.Y.; Zhang, X.; Lou, X.W. Formation of nickel cobalt sulfide ball-in-ball hollow spheres with enhanced electrochemical pseudocapacitive properties. *Nat. Commun.* **2015**, *6*, 6694. [CrossRef] [PubMed]
10. Vadivel, S.; Maruthamani, D.; Yangjeh, A.H.; Paul, B.; Dhar, S.S.; Selvam, K. Facile synthesis of novel $CaFe_2O_4$/g-C_3N_4 nanocomposites for degradation of methylene blue under visible-light irradiation. *J. Colloid Interface Sci.* **2016**, *480*, 126–136. [CrossRef] [PubMed]
11. Bellardita, M.; Paolaa, A.D.; Megna, B.; Palmisano, L. Determination of the crystallinity of TiO_2 photocatalysts. *J. Photochem. Photobiol. A* **2018**, *367*, 312–320. [CrossRef]
12. Huang, W.C.; Ting, J.M. Novel nitrogen-doped anatase TiO_2 mesoporous bead photocatalysts for enhanced visible light response. *Ceram. Int.* **2017**, *43*, 9992–9997. [CrossRef]
13. Qi, D.P.; Zheng, L.Y.; Cao, X.B.; Jiang, Y.Y.; Xu, H.B.; Zhang, Y.Y.; Yang, B.J.; Sun, Y.H.; Hng, H.H.; Lu, N.; et al. Bio-inspired antireflective hetero-nanojunctions with enhanced photoactivity. *Nanoscale* **2013**, *5*, 12383–12387. [CrossRef] [PubMed]
14. Wang, L.; Kumeria, T.; Santos, A.; Forward, P.; Lambert, M.F.; Losic, D. Iron oxide nanowires from bacteria biofilm as an efficient visible-light magnetic photocatalyst. *ACS Appl. Mater. Interfaces* **2016**, *8*, 20110–20119. [CrossRef] [PubMed]
15. Rashid, J.; Barakat, M.A.; Mohamed, R.M.; Ibrahim, I.A. Enhancement of photocatalytic activity of zinc/cobalt spinel oxides by doping with ZrO_2 for visible light photocatalytic degradation of 2-chlorophenol in wastewater. *J. Photochem. Photobiol. A Chem.* **2014**, *284*, 1–7. [CrossRef]
16. Chen, J.; Zhan, J.; Lu, E.; Wan, Y.; Jin, Z.; Qi, H. Facile template-free fabrication of mesoporous $ZnCo_2O_4$ fibers with enhanced photocatalytic activity under visible-light irradiation. *Mater. Lett.* **2018**, *220*, 66–69. [CrossRef]
17. Wang, B.; Wang, Y.; Lei, Y.; Wu, N.; Gou, Y.; Han, C.; Xie, S.; Fang, D. Mesoporous silicon carbide nanofibers with in situ embedded carbon for co-catalyst free photocatalytic hydrogen production. *Nano Res.* **2016**, *9*, 886–898. [CrossRef]

18. Jiang, L.; Yuan, X.; Zeng, G.; Wu, Z.; Liang, J.; Chen, X.; Leng, L.; Wang, H.; Wang, H. Metal-free efficient photocatalyst for stable visible-light photocatalytic degradation of refractory pollutant. *Appl. Catal. B* **2018**, *221*, 715–725. [CrossRef]
19. Wang, W.; Yu, Y.; An, T.; Li, G.; Yip, H.Y.; Yu, J.C.; Wong, P.K. Visible-Light-Driven Photocatalytic Inactivation of *E. coli* K-12 by Bismuth Vanadate Nanotubes: Bactericidal Performance and Mechanism. *Environ. Sci. Technol.* **2012**, *46*, 4599–4606. [CrossRef] [PubMed]
20. Cheng, H.; Huang, B.; Dai, Y.; Qin, X.; Zhang, X. One-Step Synthesis of the Nanostructured AgI/BiOI Composites with Highly Enhanced Visible-Light Photocatalytic Performances. *Langmuir* **2010**, *26*, 6618–6624. [CrossRef] [PubMed]
21. Jo, W.; Natarajan, T. Influence of TiO_2 morphology on the photocatalytic efficiency of direct Z-scheme g-C_3N_4/TiO_2 photocatalysts for isoniazid degradation. *Chem. Eng. J.* **2015**, *281*, 549–565. [CrossRef]
22. Tan, Y.; Lin, Z.; Ren, W.; Long, W.; Wang, Y.; Ouyang, X. Facile solvothermal synthesis of Cu_2SnS_3 architectures and their visible-light-driven photocatalytic properties. *Mater. Lett.* **2012**, *89*, 240–242. [CrossRef]
23. Vadivel, S.; Maruthamani, D.; Paul, B.; Dhar, S.S.; Yangjeh, H.A.; Balachandran, S.; Saravanakumar, B.; Selvakumar, A.; Selvam, K. Biomolecule-assisted solvothermal synthesis of Cu_2SnS_3 flowers/RGO nanocomposites and their visible-light-driven photocatalytic activities. *RSC Adv.* **2016**, *6*, 74177–74185. [CrossRef]
24. Yao, S. Enhanced photocatalytic degradation of Rhodamine B by reduced graphene oxides wrapped-Cu_2SnS_3 flower-like architectures. *J. Alloys Compd.* **2017**, *704*, 469–477. [CrossRef]
25. Vadivel, S.; Paul, B.; Habibi-Yangjeh, A.; Maruthamani, D.; Kumaravel, M.; Maiyalagan, T. One-pot hydrothermal synthesis of $CuCo_2S_4$/RGO nanocomposites for visible-light photocatalytic applications. *J. Phys. Chem. Solids* **2018**, *123*, 242–253. [CrossRef]
26. Meng, Z.; Ullah, K.; Zhu, L.; Ye, S.; Oh, W. Modified hydrothermal fabrication of a CoS_2–graphene hybrid with improved photocatalytic performance. *Mater. Sci. Semicond. Process.* **2014**, *27*, 173–180. [CrossRef]